1   **How Friction Starts: Nucleation fronts initiate frictional motion**

2   Shahar Gvirtzman & Jay Fineberg

3   *The Racah Institute of Physics, The Hebrew University of Jerusalem, Givat Ram 91904, Israel*

4   **Rapid rupture fronts[1–5], akin to earthquakes, mediate the transition to frictional motion. Once formed,**

5   **their singular form[1,3,6–11], dynamics[12,13]and arrest[2,14] are well-described by fracture mechanics. Ruptures,**

6   **however, first need to be created within initially rough frictional interfaces. Hence, ``static friction**

7   **coefficients" are not well-defined; frictional ruptures nucleate over a wide range of applied forces[4,9,15,16].**

8   **A critical open question is, therefore, how the nucleation of rupture fronts actually takes place[17–23].**

9   **Here, we experimentally show that rupture fronts are prefaced by slow nucleation fronts; self-similar**

10   **entities not described by fracture mechanics. They emerge from initially rough frictional interfaces at a**

11   **well-defined stress threshold, evolve at characteristic velocity and time scales governed by stress levels,**

12   **and propagate within a frictional interface to form the initial rupture from which fracture mechanics**

13   **take over. These results are of fundamental importance to questions ranging from earthquake**

14   **nucleation and prediction to processes governing material failure.**

15   The question of rupture nucleation has a long history. The existence of a crack in a stressed brittle material

16   creates singular stress fields having the form $1/r^{1/2}$, where r is the distance from the crack's tip. Crack

17   propagation in perfect materials initiates only when a crack surpasses a critical length, the Griffith length,

18   which is determined by geometry and applied stresses[24]. Below this length, crack propagation should not

19   occur. Beyond this length, the energy concentrated at a crack's tip becomes larger than that needed to

20   create more surface (the 'fracture energy') and cracks will propagate – generally accelerating rapidly to

21   near sonic speeds. To lose stability to *fracture*, a material must, therefore, possess a defect or a 'seed

22   crack' of size *larger* than the Griffith length.

23   Will brittle materials fracture when sufficiently large seed cracks do not exist? In the tensile fracture of

24   heterogeneous materials, statistical coalescence of microscopic cracks[25,26] surrounding the tip of cracks

25   that are nearly the Griffith length can cause material failure. Similarly, shear fracture in (heterogeneous)

26   rock can occur by the sporadic growth and coalescence of material flaws[27]. The details of these nucleation

27   processes, i.e. how small incipient cracks grow to surpass the Griffith length, are largely unknown.

28   Let us now consider a frictional interface. Frictional interfaces are inherently heterogeneous; these rough

29   interfaces are composed of ensembles of relatively sparse interconnecting contacts that bridge any two

30   contacting bodies[28]. Experiments have shown that the breakdown of a frictional interface is actually a

31   fracture problem[29,30]; sliding only takes place when the contacts are broken by coherent fronts whose

32   dynamics and structure are those of shear cracks[1,3,6,8,10]. Such interface cracks can be either rapid

33   ('seismic') and approach the Rayleigh wave speed, c_R, or even quite slow[12,31,32] (~$0.02c_R$). While the latter

34   are 'aseismic' (their slow acceleration produces a negligible seismic signature), so long as they are beyond

35   the Griffith length, they are still quantitatively described by fracture mechanics[12]. Slow propagation[12,31]

36   in the framework of fracture mechanics will occur if crack lengths barely exceed the Griffith length. Stress

37   heterogeneities or variation of the fracture energy can even cause interface cracks to arrest[2,14]. An open

38   question is whether *all* slow interface ruptures associated[19,30,33,34] with aseismic precursory motion within

39 natural faults can be addressed by fracture mechanics. While some material-independent scenarios exist
40 for propagation below the Griffith length[17,34,35] clear experimental measurements are lacking.

41 Here we address the question of how frictional cracks nucleate, since, for rough interfaces, no initial crack
42 that is close to the Griffith length exists. Simplistic nucleation criteria (e.g. a `static friction coefficient')
43 are invalid[4,16]; even considering the same two blocks[15] nucleation of interface cracks may occur for "static
44 friction coefficients" that vary by factors of 5 for, ostensibly, identical nominal conditions. Experiments[5,18–
45 22,33] have observed that very slow 'aseismic' processes often preface the rapid interface break-down
46 ('seismic' processes) that leads to frictional motion, but the form that these processes take is unclear.
47 Numerical observations assuming velocity[36] or slip[37] weakening friction laws have also observed slow
48 nucleation preceding rapid rupture, with no qualitative difference[36] between the nucleation phases of
49 small and large rupture events. Recent theoretical work[17] suggests a well-defined mechanism for
50 nucleation; slow nucleation fronts, triggered at a well-defined critical shear stress threshold, whose
51 dynamics are unrelated to fracture mechanics.

52 Despite their importance, the *mechanisms* that gives rise to frictional (and earthquake[38]) nucleation have
53 been incredibly elusive. The main reasons for this lie precisely in the unpredictability of the nucleation
54 process; our inability to control the nucleation location and conditions at the point of nucleation, with the
55 high spatial precision required, has impeded controlled studies of these critical processes.

56 By implementing a method that enables precise control of the location and stress conditions at the
57 nucleation location, we will experimentally demonstrate that the nucleation process occurs only when
58 applied stresses surpass a well-defined (but interface topography-dependent) threshold. At this point,
59 nucleation fronts are excited that are unrelated to dynamic fracture. They are extremely slow while
60 evolving and propagating at stress-dependent time scales. These fronts set the stage for the dynamic
61 ruptures governed by fracture mechanics.

62 Our experimental system[1], shown schematically in Fig. 1a, consists of 2 PMMA blocks that are pressed
63 together to form a frictional interface (Methods). Throughout each experiment, we continuously measure
64 the real contact area $A(x,z,t)$ over the entire interface every $1.7\mu s$, by an optical method based on total
65 internal reflection[32]. The interface, of width $w = 5.5mm$ and length $200mm$ consists of randomly
66 distributed contacts with roughness $\sim 3\mu m$. At selected locations, x_0, we use a marker to create 1-4mm
67 thick `barriers', oriented along the z direction, whose fracture energy is about 5 times that of the bare
68 interface (Extended Data Fig. 1). After application of a constant normal load F_N (4.5 MPa), we quasi-
69 statically increased the applied shear, F_S, until initial ruptures fronts (Fig. 1b) nucleated at $x = 0$ and
70 propagated in the positive x direction. These initial ruptures accelerate to velocities, v_{arr}, before abruptly
71 arresting[2,14] upon encountering the near side of a barrier. At later times, new rupture fronts will nucleate
72 at well-defined locations near the barrier's far side.

73 Examples of rupture arrest and subsequent nucleation are presented in Fig. 1c. While rupture arrests are
74 abrupt, it is clear that the time required for nucleation is strongly dependent on the velocity, v_{arr}, of the
75 initial ruptures immediately preceding their arrest. Moreover, as we will show, the stress conditions and
76 nucleation times are determined by v_{arr}, which range up to the Rayleigh wave speed, c_R=1255 m/s. The

higher v_{arr}, the shorter the nucleation time. Furthermore, *no* nucleation takes place (Fig. 1c –left panel)
78 for v_{arr} below location-dependent threshold values.
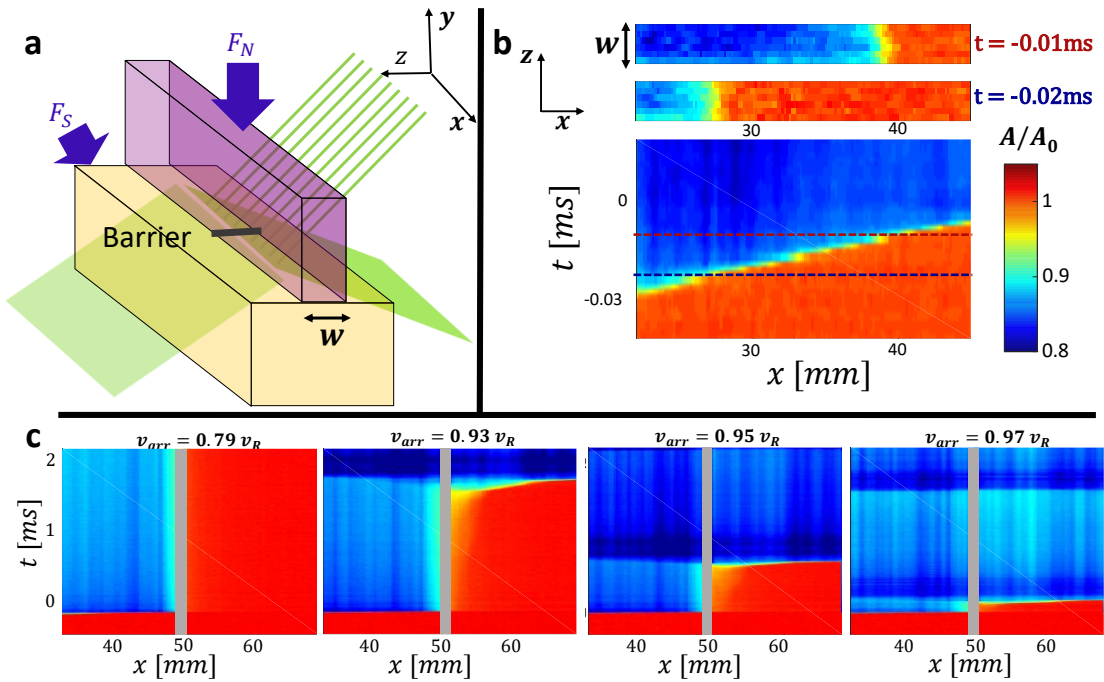
Figure 1. Experimental setup and rupture arrest by imposing barriers. a, The real contact area, $A(x,z,t)$, (width $w = 5.5mm$ and length $200mm$) forming the frictional interface between two PMMA blocks is measured every $1.7\mu s$ by an incoherent light sheet using the total internal reflection method (Methods). A high fracture energy barrier of width $\sim 1 - 4mm$ was imprinted across the interface (gray line). **b,** (top) $A(x,z,t)$ of a typical rupture front at the onset of stick-slip motion at times $10\mu s$ apart. (bottom) Full spatiotemporal dynamics of the contact area, averaged over the z axis. $A(x,z,t)$ is normalized by $A_0 = A(x,z,t_0)$, where t_0 is a time prior to rupture propagation. Dashed lines denote the times of the snapshots in the top panel. **c,** Examples where spontaneously nucleated ruptures arrest at a barrier located at $x_0 = 50$mm (grey boxes) . Noted are their propagation velocities, v_{arr}, at arrest. Arrested ruptures may trigger the nucleation of a new rupture on the far side of the barrier. The duration of the nucleation process decreases with increasing v_{arr}. Below a threshold value of v_{arr} (left panel) arrested ruptures will not nucleate another rupture.

In Fig. 2 we focus on the short-time effects of the sudden rupture arrest on the nucleation area. Each rupture arrest produces a wave that propagates at approximately the shear wave velocity, C_S, that, within $\sim 10\mu s$ of its passage, reduces $A(x,t) \equiv < A(x,z,t) >_z$ by 1-2% in a 'damage zone' that extends a few mm's beyond the far side of the barrier. The damage zone is indicated by a sharp drop of $A(x,t)$ followed by a region of gradually decreasing damage. We utilize the edge of the sharp reduction of $A(x,t)$ to characterize the extent of the damage zone, ξ_0 (Fig. 2b). ξ_0 is defined as the point where $A(x)$ falls below the gradual damage level by 2 standard deviations of the measurement noise (Methods). The amount of the initial damage, D, increases with v_{arr}, as shown in Figs. 2c,d. Damage jumps, $D(v_{arr})$, occur within $\sim 10 \mu s$ of rupture arrest. After that, $D(v_{arr})$ are stable, with only slight fluctuations resulting from wave reflections from the block boundaries. It is interesting that the size of ξ_0 is nearly independent of v_{arr} (inset) and consistent with the nonlinear scale preceding rupture tips identified in recent cohesive zone

102 measurements[39]. Furthermore, while damage always takes place, rupture nucleation does not always
103 occur; blue symbols in Fig. 2c,d denote arrest events that did *not* nucleate.

104

105
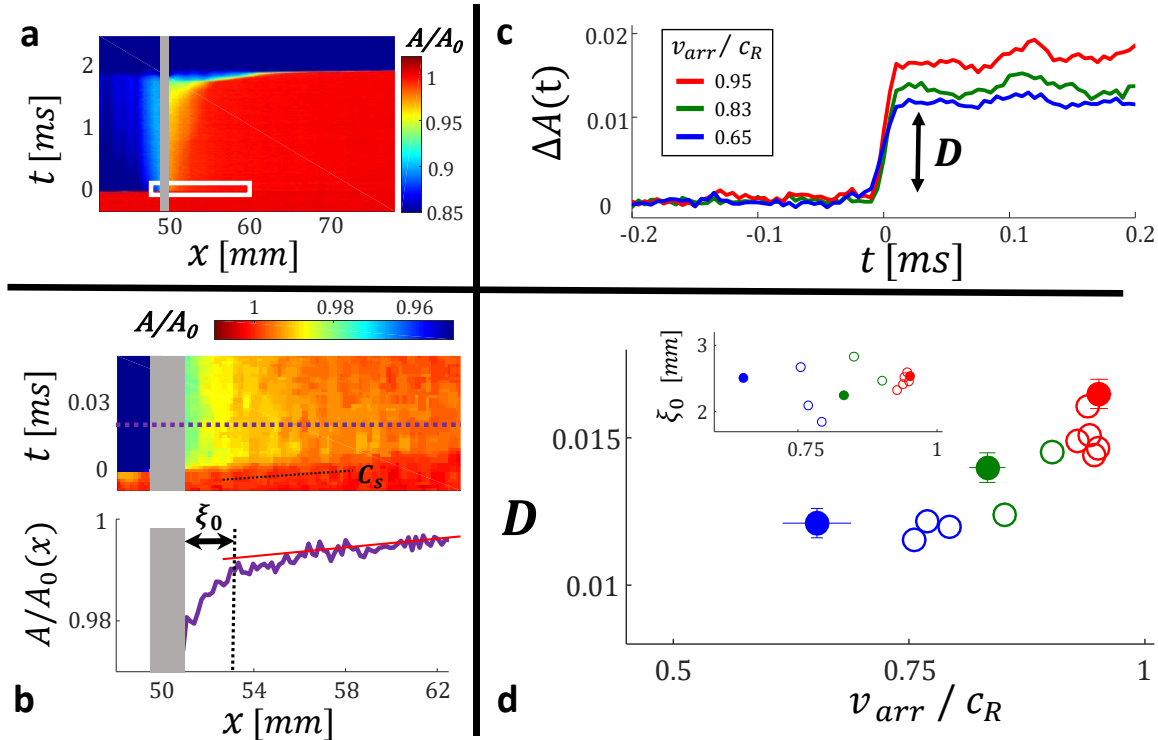
Figure 2. Rupture arrest generates initial damage ahead. a, Spatiotemporal dynamics of a typical nucleation process
upon arrest of an impinging rupture. (imposed barrier in gray) **b,** (top) Close-up of $A(x,t)$ upon crack arrest. (white
rectangle in **a**) showing the passage of a wave (velocity $\sim C_S$) generated by the arrested rupture. This wave triggers
damage (reduced $A(x,t)$) in a zone extending a distance ξ_0 from the far side of the barrier. (bottom) The damage
zone size, ξ_0, is evident from the instantaneous spatial profile, $A(x,t)$, of the contact area at time $t = 0.02ms$
(dashed line in top panel). ξ_0 is defined as the point where the distance between the measurements and
extrapolated fit (red line) of values of $\langle A(x) \rangle$ far from the barrier exceeds 2 standard deviations. Here, $\langle A(x) \rangle$ is the
time averaged contact area within the temporally stationary damage zone (Methods). **c,** $A(x,t)$ jumps upon
passage of the shear wave. Shown are $\Delta A(t) = \langle 1 - A /A_0 \rangle_{z,x<\xi_0}$ from 3 events with different v_{arr}. We define the
initial damage for each event, D, as the jump in $\Delta A(t)$. **d,** D dependence on v_{arr}. While D, clearly increases with
v_{arr}, the damage zone size, ξ_0, (inset) does not. Symbol colors: (blue) events that didn't form nucleation fronts,
(red) events that nucleated and reached dynamic rupture, (green) events that formed nucleation fronts that
triggered arrested dynamic ruptures. Filled circles: the events presented in (c).

119 If a new crack is nucleated, nucleation will occur on the far side of the barrier (Fig. 1c), as the contacts on
120 the far side of the barrier are both damaged (Fig. 2) and experience high shear stresses remotely imposed
121 by the arrested initial crack. Knowledge of the nucleation location enables us to focus on the nucleation
122 process and track the formation of the new rupture front.

123 After a static 'damage' stage, where the spatial extent of ξ_0 is stationary, nucleation fronts, defined by
124 the propagating edges of the damage zone in the x direction, $\xi(t)$, form within the weakened area and
125 slowly expand in space. An example of the nucleation phase is presented in Fig 3. After an initial period

126 where $\xi(t) = \xi_0$, (blue lines in Fig. 3a) the regions of reduced $A(x,t)$ slowly expand and deepen. $\xi(t)$
127 is indicated by the brown profiles in Fig. 3a. $v_{nuc} \equiv d\xi/dt$, the nucleation front velocities, are extremely
128 slow ($1 < v_{nuc} < 10ms^{-1}$) and nearly constant over the 3-4mm length of the nucleation zone. The slow
129 expansion characterized by v_{nuc} simultaneously takes place in the z direction. Defining $\delta_z(t)$ as the mean
130 width in z of the nucleation zone (Methods and Fig. 3b), we find that both $\xi(t)$ and $\delta_z(t)$ expand at
131 about the same rate, as is evident in the typical 2D dynamics presented in Fig. 3b and quantified in Fig.
132 3c. This slow 2D propagation continues until losing stability, at a time τ after the damage onset (Fig. 2).
133 At $t = \tau$ nucleation fronts abruptly undergo rapid acceleration (Fig. 3c) that signals the onset of dynamic
134 rupture. Here, ruptures become shear cracks[1] whose dynamics are described by fracture mechanics[12].
135 Dynamic ruptures continuously accelerate to propagation velocities about 2 orders of magnitude greater
136 than v_{nuc}.
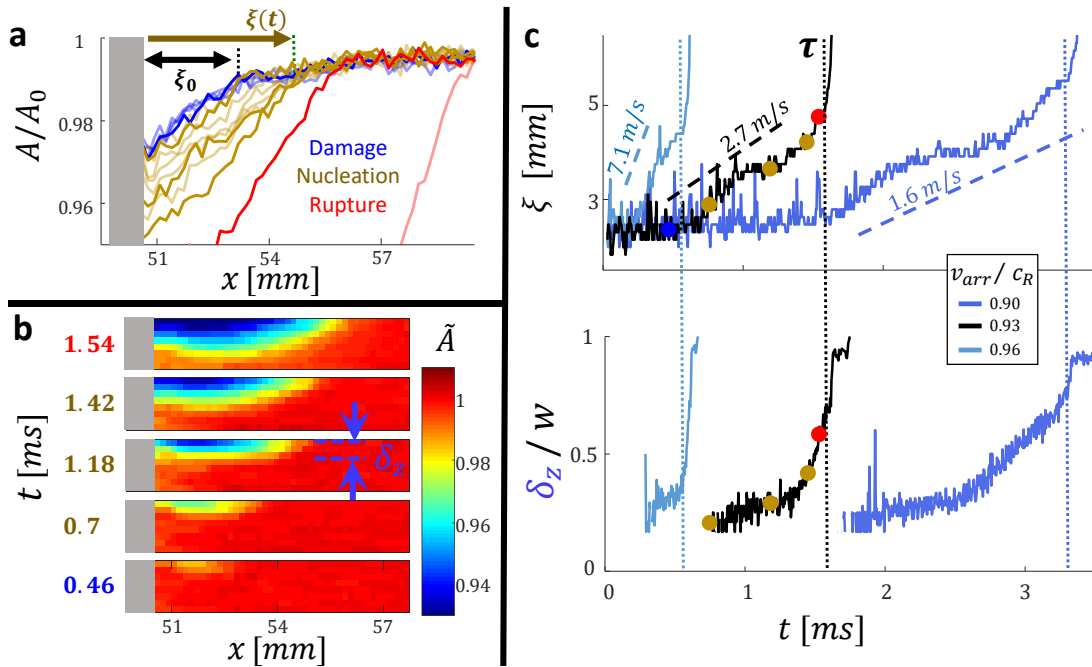
137
138 **Figure 3. Nucleation is mediated by slowly propagating nucleation fronts**. **a,** Successive profiles (intervals of
139 0.12ms) of $A(x,t)$ showing the transition from the static damage phase (blue) to slow propagation of a nucleation
140 front (brown) that triggers dynamic rupture (red). $\xi(t)$, denoting the leading edge of the nucleation front, is defined
141 like ξ_0 in Fig. 2. **b,** $\tilde{A}(x,z,t)$ shows the slow 2D evolution of the nucleation front, normalized after the initial damage
142 triggered by the rupture arrest at $t = 0$. Snapshots correspond to bold profiles in (a). **c,** Propagation of nucleation
143 fronts for 3 events in (top) x, and (bottom) z. $\delta_z(t)$ is the mean width (in z) of a rupture front (see (b) and Methods).
144 w is the sample width. Black curves describe the event in (a,b); circles mark the snapshots in (b). The timescale, τ,
145 of each event is defined by the sharp onset of the rapid accelerations of $\xi(t)$ (dotted lines) that mark the initiation
146 of dynamic rupture. Dashed lines: mean nucleation-front velocities, v_{nuc}.

147 What governs the values of τ? Fig. 3c suggests that τ decrease with v_{arr}. Using fracture mechanics, we
148 can relate v_{arr} to the magnitude of the induced shear stress field, $\sigma_{ind}(r) \propto K(v_{arr}) \cdot r^{-1/2}$, created
149 ahead of the barrier by the arrested ruptures, where K is the stress intensity factor[24] (Methods).
150 Nucleation always takes place within the initial damage zone ($x < \xi_0$), but its precise location is difficult
151 to identify. We, therefore, define the nucleation point as the center of the damage zone ($\xi_0/2$ from the

152 barrier's far side (Fig. 4a)). $\sigma_{ind}(r^*)$ approximates the stress field at the nucleation point, whose distance
153 is r^* from the arrested crack tip. In Fig. 4b we compare 3 different sets of experiments conducted under
154 similar conditions (using the same samples and normal load). The sets differed in the barrier (arrest)
155 location and barrier width imposed (Fig. 1). Each barrier location triggered nucleation within a different
156 region within the interface, resulting in a different r* values and ranges of v_{arr} obtained (inset Fig. 4b).
157 In each of these, we computed the value of $K(v_{arr})$ at the rupture arrest (Methods). This procedure
158 enables the comparison (Fig. 4b) of $\sigma_{ind}(r^*)$ vs. τ for each data set. In all sets, τ is a continuous function
159 of $\sigma_{ind}(r^*)$ with an approximate dependence $\sigma_{ind}(r^*) \propto 1/\tau$. Moreover, while the proportionality
160 factor varied with the barrier location, all experiments yielded a distinct (location – dependent) *threshold*,
161 σ_{thresh}, below which no nucleation front was excited.
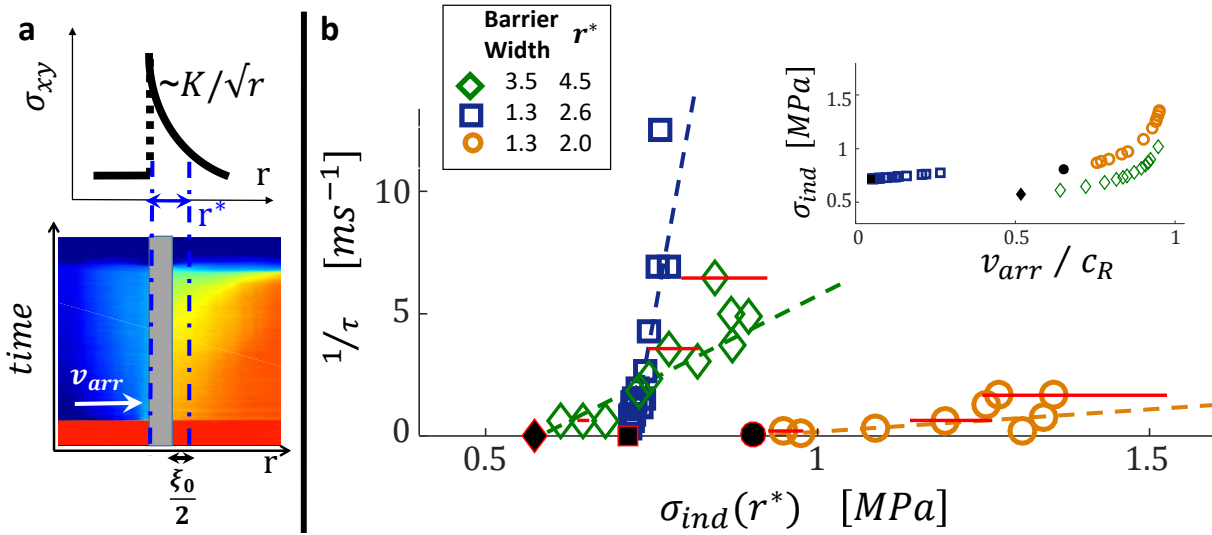
162

163

164 **Figure 4. The shear stress level determines the nucleation time, τ. a,** We used fracture mechanics to relate v_{arr}
165 to the magnitude, K, of the stress singularity created by the barrier-arrested rupture, hence the induced stress,
166 $\sigma_{ind}(r^*)$, at the nucleation point, r^* (distance from the arrest point to the damage zone center, $\xi_0/2$ from the
167 barrier). **b,** τ dependence on σ_{ind}. Shown are many events from experiments performed under similar conditions
168 at barrier locations, 100mm (squares), 70mm (diamonds), and 50mm (circles). The latter data set was used in Figs.
169 1-5. Dashed lines are guides for extrapolation to $\tau \to \infty$. Black shapes: Highest $\sigma_{ind} \le \sigma_{thresh}$ for which *no*
170 nucleation front was observed, within the 15ms limits set by our experimental apparatus. The longest value of τ
171 observed was 9ms; values of τ spanned over 1 (circles, diamonds) to 2 (squares) orders of magnitude. Typical error
172 bars correspond to our $20-30ms^{-1}$ resolution in v_{arr}. Noted are the values of r^* measured for each barrier. (inset)
173 σ_{ind} as determined by v_{arr}.

174 The timescale τ characterizes the nucleation process. In Fig. 5 we show that all dynamic quantities
175 measured within the nucleation process are governed by this single timescale, which can span over an
176 order of magnitude. $\xi(t)$ and $\delta_z(t)$ describe locations of the leading edges of the front, while $\Delta A(t) \equiv$
177 $1 - \langle A(x,t)/A_0 \rangle_{z, x < \xi_0}$ describes the contact area reduction at the 'tail' of the front, within the initial
178 damage zone (Fig. 2). $\Delta A(t)$ increases continuously until the onset of dynamic rupture at $t = \tau$. As Fig. 5
179 demonstrates, when t is scaled by τ, the evolutions of *all* of these independent quantities collapse to well-

180 defined (local topography-dependent) functions for $t < 0.8 \cdot \tau$ for each of the different experiments
181 presented in Fig. 4b.

182 The data collapse evident for $t < \tau$ breaks down, once dynamic fracture initiates. In Fig. 5 events where
183 nucleation fronts triggered dynamic ruptures are denoted by shades of red. For comparison, we also
184 include an example (blue) where no nucleation front was excited as well as examples (green) for which
185 rupture fronts eventually arrested. The instability point at $\xi(t = \tau)$, which depends on the barrier
186 location, is where dynamic fracture initiates. The breakdown of the scaling of $\xi(t)$, $\delta_z(t)$ and $\Delta A(t)$ at
187 this point suggests that the nucleation process is indeed disassociated from that of dynamic rupture; for
188 $x < \xi(\tau)$ all nucleation fronts behave in the same way, whereas for $x > \xi(\tau)$ front dynamics are
189 governed by fracture mechanics[12]. In the borderline cases (green in Fig. 5) fronts arrest beyond τ, possibly
190 due to either local fracture energy barriers or aging processes[40] that are important at time scales $> 1ms$.
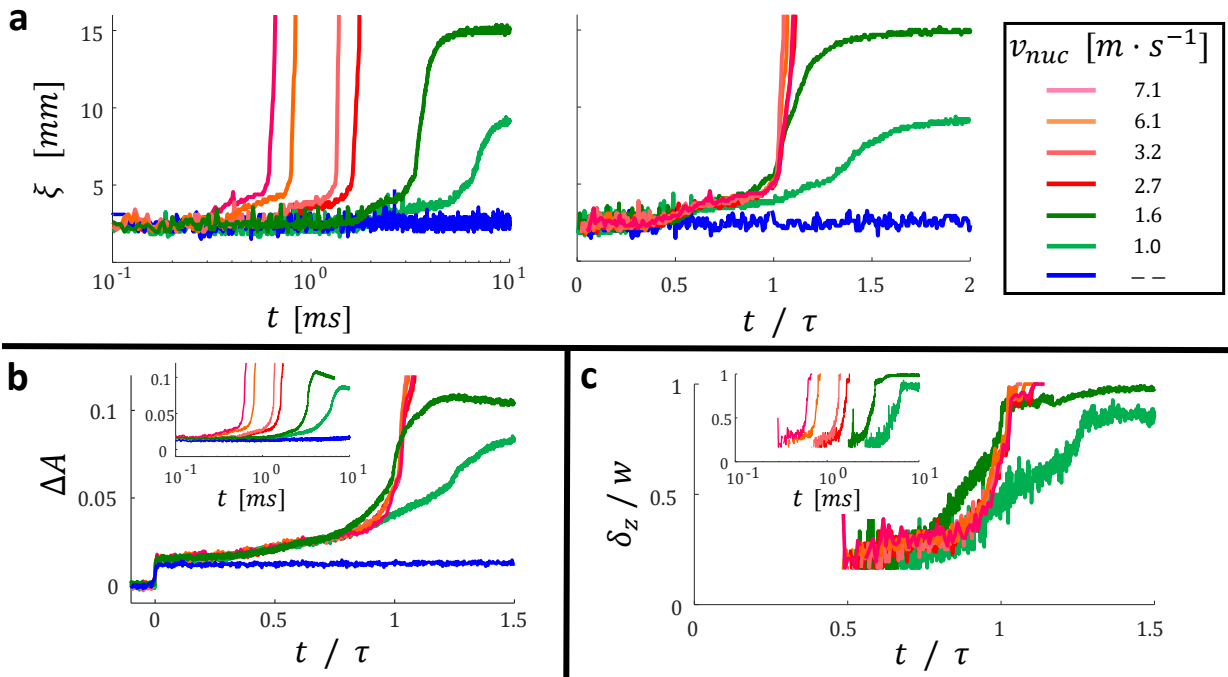
191
192 **Figure 5. Nucleation dynamics scale with the nucleation time, τ. a.** (left) Nucleation front propagation in the x
193 direction, $\xi(t)$, for events at the same (50mm) barrier location with $1.0 < v_{nuc} < 7.1 \; ms^{-1}$. (right) When scaled
194 by τ, $\xi(t/\tau)$ collapse to a single form for $t < 0.8 \cdot \tau$. (blue) no nucleation and (green) nucleation fronts that either
195 arrested beyond τ or (red) developed to fully dynamic ruptures. **b,** Contact area levels at the 'tail' of the front,
196 $\Delta A(t/\tau) \equiv 1 - \langle A(x, t/\tau)/A_0 \rangle_{z,x < \xi_0}$, **c,** nucleation front propagation in the z direction, $\delta_z(t/\tau) / w$, for the same
197 events (See Fig. 2) . Insets are respective unscaled data. Note that during dynamic rupture ($t > \tau$), when the
198 dynamics are governed by fracture mechanics, no such scaling is observed.

199 We have used the stress transfer resulting from arrested ruptures to show that nucleation fronts are well-
200 defined vehicles that create the conditions enabling rapid interface rupture. The transferred stress first
201 weakens the nucleation area (Fig. 2) and then drives the nucleation process (Fig. 4). Such stress transfer
202 is also believed to drive "remote triggering" of natural earthquakes[41].

203

204   We have seen that nucleation fronts are 'inertia-less', propagating slowly at approximately constant
205   (stress-dependent) velocities. We have also seen that, upon surpassing a nucleation length, $\xi(t = \tau) -$
206    $\xi_0/2$, these fronts undergo abrupt transitions to the rapidly accelerating, inertially driven, high speed
207   rupture fronts that are identified with shear cracks. These nucleation lengths range from 3 to 8 mm and
208   closely correspond to Griffith lengths (Methods and Extended Data Figures 2 and 3) calculated using
209   fracture mechanics. We, therefore, identify nucleation lengths with the corresponding Griffith lengths,
210   L_G. This identification, together with the inertia-less dynamics of the nucleation fronts, may also provide
211   a plausible explanation for the linear relation between τ^{-1} and $\sigma_{ind} - \sigma_{thresh}$ in Fig. 4b (Methods).

212   Our observations of scaling behavior and inertia-less propagation that takes place significantly below
213   L_G clearly demonstrate that nucleation fronts are wholly different entities than the rupture fronts
214   described by fracture mechanics. These qualities are consistent with recent predictions[17] of distinct
215   nucleation fronts with a major difference; while both are excited beyond a clear threshold, theoretical
216   predictions anticipate that this threshold is *above* L_G, in contrast to experimentally observed fronts.

217   Beyond L_G, a transition from 2D to 1D fronts (i.e. $\delta_z \to w$) occurs where additional jumps in rupture
218   velocity are observed, as in recent experiments[23,42]. We ascribe this to geometrical considerations
219   (Methods) and not to new physics. It is noteworthy that the Griffith length is about 100 times smaller
220   than critical rupture lengths predicted via "Rate and State" friction[43] and an order of magnitude lower
221   than predicted by friction laws incorporating slip weakening[37] (Methods).

222   Details like the front shapes, their explicit stress dependence and stress thresholds, however, *do* depend
223   on nucleation locations, as in the different experiments presented in Fig. 4. These differences indicate the
224   importance of the discrete nature of the interface and its local topography (which determines the fracture
225   energy landscape). The discrete nature of frictional interfaces may be intimately related to the mechanism
226   that drives nucleation fronts[34,35]. An interesting open question is whether this mechanism is related to
227   mechanisms[34] used to model experimentally observed slow fronts in which the discrete nature of the
228   interface plays a key role. Whether a slow front is below or above the Griffith length has a critical effect
229   on both how they are driven as well as their consequent dynamics[17,34].

230   We have characterized a new mechanism for the nucleation of frictional ruptures, a system that is
231   important in its own right as well as in analogous natural settings, such as earthquake nucleation. One
232   characteristic of these extremely slow nucleation fronts is that they are inherently aseismic[22]. Within
233   natural faults, we would therefore expect their excitation to be accompanied by a pronounced reduction
234   of background seismicity near hypocenters of emerging earthquakes. The general type of nucleation
235   process described here, may also provide insight to the more general question of how the onset of
236   fracture takes place. This, despite much work[26], still remains a challenge to our fundamental
237   understanding of material stability.

240   **Author Contributions:** SG performed the experimental measurements. SG and JF contributed to the data
241   analysis, experimental design and writing of the manuscript.

Methods Summary:

The Methods section includes descriptions of the sample construction, measurements, loading system and experimental protocol. Also included are descriptions of the influence of the marker on the fracture energy, and how we determined the quantities v_{arr}, $\Delta A(t)$, $\xi(t)$, τ, and σ_{ind}. We also include descriptions of the Griffith length calculation and our estimation of the critical nucleation length using Rate and State and Slip Weakening friction parameters. We additionally include an explanation of the linear relation between τ^{-1} and σ_{ind}. Extended Data Figures 1-3 are contained in this section.

Extended Data Figure 1: Fracture energy increase by the marker layer.

Extended Data Figure 2: Calculation of theoretical stress intensity factors.

Extended Data Figure 3. Comparison of theoretical and measured Griffith lengths.

Data Availability

Source data for Figs. 2c,d, 3a,c,d, 4b and 5 are available with this paper. All other data that support the plots within this paper and other findings of this study are available from the corresponding author upon request.

References

1.   Svetlizky, I. & Fineberg, J. Classical shear cracks drive the onset of dry frictional motion. *Nature* **509**, 205–208 (2014).

2.   Bayart, E., Svetlizky, I. & Fineberg, J. Fracture mechanics determine the lengths of interface ruptures that mediate frictional motion. *Nat. Phys.* **12**, 166-+ (2016).

3.   Mello, M., Bhat, H. S. & Rosakis, A. J. Spatiotemporal properties of Sub-Rayleigh and supershear rupture velocity fields: Theory and experiments. *J. Mech. Phys. Solids* **93**, 153–181 (2016).

4.   Passelègue, F. X., Schubnel, A., Nielsen, S., Bhat, H. S. & Madariaga, R. From Sub-Rayleigh to Supershear Ruptures During Stick-Slip Experiments on Crustal Rocks. *Science* **340**, 1208–1211 (2013).

5.   Nielsen, S., Taddeucci, J. & Vinciguerra, S. Experimental observation of stick-slip instability fronts. *Geophys. J. Int.* **180**, 697–702 (2010).

6.   Shlomai, H., Kammer, D. S., Adda-Bedia, M. & Fineberg, J. The onset of the frictional motion of dissimilar materials. *Proc. Natl. Acad. Sci. U. S. A.* **117**, 13379–13385 (2020).

7.   Svetlizky, I. *et al.* Properties of the shear stress peak radiated ahead of rapidly accelerating rupture fronts that mediate frictional slip. *Proc. Natl. Acad. Sci. U. S. A.* **113**, 542–547 (2016).

8.   Xu, S., Fukuyama, E. & Yamashita, F. Robust Estimation of Rupture Properties at Propagating Front of Laboratory Earthquakes. *J. Geophys. Res. Solid Earth* **124**, 766–787 (2019).

9.   Passelègue, F. X. *et al.* Initial effective stress controls the nature of earthquakes. *Nat. Commun.* **11**, 5132 (2020).

276   10.   Svetizky, I., Albertini, G., Cohen, G., Kammer, D. S. & Fineberg, J. Dynamic fields at the tip of sub-
277   Rayleigh and supershear frictional rupture fronts. *J. Mech. Phys. Solids* **137**, 103826 (2020).

278   11.   Kammer, D. S. & McLaskey, G. C. Fracture energy estimates from large-scale laboratory
279   earthquakes. *Earth Planet. Sci. Lett.* **511**, 36–43 (2019).

280   12.   Svetlizky, I., Kammer, D. S., Bayart, E., Cohen, G. & Fineberg, J. Brittle Fracture Theory Predicts
281   the Equation of Motion of Frictional Rupture Fronts. *Phys. Rev. Lett.* **118**, 125501 (2017).

282   13.   Kammer, D. S., Svetlizky, I., Cohen, G. & Fineberg, J. The equation of motion for supershear
283   frictional rupture fronts. *Sci. Adv.* **4**, eaat5622 (2018).

284   14.   Bayart, E., Svetlizky, I. & Fineberg, J. Rupture Dynamics of Heterogeneous Frictional Interfaces. *J.
285   Geophys. Res.-Solid Earth* **123**, 3828–3848 (2018).

286   15.   Ben-David, O., Cohen, G. & Fineberg, J. The Dynamics of the Onset of Frictional Slip. *Science* **330**,
287   211–214 (2010).

288   16.   Ben-David, O. & Fineberg, J. Static Friction Coefficient Is Not a Material Constant. *Phys. Rev. Lett.*
289   **106**, 254301 (2011).

290   17.   Brener, E. A., Aldam, M., Barras, F., Molinari, J.-F. & Bouchbinder, E. Unstable Slip Pulses and
291   Earthquake Nucleation as a Nonequilibrium First-Order Phase Transition. *Phys. Rev. Lett.* **121**, 234302
292   (2018).

293   18.   Latour, S., Schubnel, A., Nielsen, S., Madariaga, R. & Vinciguerra, S. Characterization of
294   nucleation during laboratory earthquakes. *Geophys. Res. Lett.* **40**, 5064–5069 (2013).

295   19.   Dresen, G., Kwiatek, G., Goebel, T. & Ben-Zion, Y. Seismic and Aseismic Preparatory Processes
296   Before Large Stick-Slip Failure. *Pure Appl. Geophys.* doi:10.1007/s00024-020-02605-x.

297   20.   Ohnaka, M. & Shen, L. F. Scaling of the shear rupture process from nucleation to dynamic
298   propagation: Implications of geometric irregularity of the rupturing surfaces. *J. Geophys. Res.-Solid Earth*
299   **104**, 817–844 (1999).

300   21.   Popov, V. L., Grzemba, B., Starcevic, J. & Fabry, C. Accelerated creep as a precursor of friction
301   instability and earthquake prediction. *Phys. Mesomech.* **13**, 283–291 (2010).

302   22.   Wu, B. S. & McLaskey, G. C. Contained Laboratory Earthquakes Ranging From Slow to Fast. *J.
303   Geophys. Res. Solid Earth* **124**, 10270–10291 (2019).

304   23.   McLaskey, G. C. Earthquake Initiation From Laboratory Observations and Implications for
305   Foreshocks. *J. Geophys. Res. Solid Earth* **124**, 12882–12904 (2019).

306   24.   Freund, L. B. *Dynamic Fracture Mechanics*. (Cambridge, 1990).

307   25.   Ciliberto, S., Guarino, A. & Scorretti, R. The effect of disorder on the fracture nucleation process.
308   *Phys. D* **158**, 83–104 (2001).

309   26.   Ramos, O., Cortet, P.-P., Ciliberto, S. & Vanel, L. Experimental Study of the Effect of Disorder on
310   Subcritical Crack Growth Dynamics. *Phys. Rev. Lett.* **110**, 165506 (2013).

311   27.   Reches, Z. & Lockner, D. A. Nucleation and growth of faults in brittle rocks. *J. Geophys. Res. Solid*
312   *Earth* **99**, 18159–18173 (1994).

313   28.   Bowden, F. P. & Tabor, D. *The Friction and Lubrication of Solids*. (Oxford Univ. Press, 2001).

314   29.   Palmer, A., C. & Rice, J., R. The Growth of Slip Surfaces in the Progressive Failure of Over-
315   Consolidated Clay. *Proc. R. Soc. Math. Phys. Eng. Sci.* **332**, 527–548 (1973).

316   30.   Barras, F. *et al.* Emergence of Cracklike Behavior of Frictional Rupture: The Origin of Stress
317   Drops. *Phys. Rev. X* **9**, 041043 (2019).

318   31.   Rubinstein, S. M., Cohen, G. & Fineberg, J. Dynamics of Precursors to Frictional Sliding. *Phys Rev*
319   *Lett* **98**, 226103 (2007).

320   32.   Rubinstein, S. M., Cohen, G. & Fineberg, J. Detachment fronts and the onset of dynamic friction.
321   *Nature* **430**, 1005–1009 (2004).

322   33.   Acosta, M., Passelegue, F. X., Schubnel, A., Madariaga, R. & Violay, M. Can Precursory Moment
323   Release Scale With Earthquake Magnitude? A View From the Laboratory. *Geophys. Res. Lett.* **46**, 12927–
324   12937 (2019).

325   34.   Trømborg, J. K. *et al.* Slow slip and the transition from fast to slow fronts in the rupture of
326   frictional interfaces. *Proc. Natl. Acad. Sci.* **111**, 8764 (2014).

327   35.   de Geus, T. W. J., Popović, M., Ji, W., Rosso, A. & Wyart, M. How collective asperity detachments
328   nucleate slip at frictional interfaces. *Proc. Natl. Acad. Sci.* **116**, 23977 (2019).

329   36.   Lapusta, N. & Rice, J. R. Nucleation and early seismic propagation of small and large events in a
330   crustal earthquake model. *J. Geophys. Res. Solid Earth* **108**, (2003).

331   37.   Uenishi, K. & Rice, J. R. Universal nucleation length for slip-weakening rupture instability under
332   nonuniform fault loading. *J. Geophys. Res.-Solid Earth* **108**, 2042 (2003).

333   38.   Kato, A. & Ben-Zion, Y. The generation of large earthquakes. *Nat. Rev. Earth Environ.* **2**, 26–39
334   (2021).

335   39.   Berman, N., Cohen, G. & Fineberg, J. Dynamics and Properties of the Cohesive Zone in Rapid
336   Fracture and Friction. *Phys. Rev. Lett.* **125**, 125503 (2020).

337   40.   Ben-David, O., Rubinstein, S. M. & Fineberg, J. Slip-stick and the evolution of frictional strength.
338   *Nature* **463**, 76–79 (2010).

339   41.   Brodsky, E. E. & van der Elst, N. J. The Uses of Dynamic Earthquake Triggering. in *Annual Review*
340   *of Earth and Planetary Sciences, Vol 42* (ed. Jeanloz, R.) vol. 42 317–339 (Annual Reviews, 2014).

341   42.   Fukuyama, E. *et al.* Spatiotemporal complexity of 2-D rupture nucleation process observed by
342   direct monitoring during large-scale biaxial rock friction experiments. *Tectonophysics* **733**, 182–192
343   (2018).

344   43.   Rice, J. R., Lapusta, N. & Ranjith, K. Rate and state dependent friction and the stability of sliding
345   between elastically deformable solids. *J. Mech. Phys. Solids* **49**, 1865–1898 (2001).

346   44.   Shlomai, H., Adda-Bedia, M., Arias, R. E. & Fineberg, J. Supershear Frictional Ruptures Along
347   Bimaterial Interfaces. *J. Geophys. Res.-Solid Earth* **125**, e2020JB019829 (2020).

348   45.   Bayart, E., Svetlizky, I. & Fineberg, J. Slippery but Tough: The Rapid Fracture of Lubricated
349   Frictional Interfaces. *Phys. Rev. Lett.* **116**, 194301 (2016).

350   46.   Tada, H., Paris, P. C. & Irwin, G. R. The Stress Analysis of Cracks Handbook, Third Edition. (2000)
351   doi:10.1115/1.801535.

352   47.   Newman, J. C. & Raju, I. S. An empirical stress-intensity factor equation for the surface crack.
353   *Eng. Fract. Mech.* **15**, 185–192 (1981).

354   48.   Dieterich, J. Modelling of rock friction:1.Experimental results and constitutive equations.
355   *JGeophys Res* **84**, 2161–2168 (1979).

356   49.   Rice, J. R. & Ruina, A. L. Stability of Steady Frictional Slipping. *J. Appl. Mech.* **50**, 343–349 (1983).

357   50.   Baumberger, T., Berthoud, P. & Caroli, C. Physical analysis of the state- and rate-dependent
358   friction law. II. Dynamic friction. *Phys. Rev. B* **60**, 3928–3939 (1999).

359   51.   Berthoud, P., Baumberger, T., G'Sell, C. & Hiver, J. M. Physical analysis of the state- and rate-
360   dependent friction law: Static friction. *Phys. Rev. B* **59**, 14313–14327 (1999).

361   52.   Schär, S., Albertini, G. & Kammer, D. S. Nucleation of frictional sliding by coalescence of
362   microslip. *ArXiv201004343 Cond-Mat* (2020).

363

364   **Methods**

365   Sample construction
366   Our samples were constructed of poly(methylmethacrylate) (PMMA) blocks. The $x \times y \times z$ dimensions
367   of the top and bottom blocks were, respectively, 200 X 100 X 5.5mm and 290 X 28 X 30mm. The top block
368   was diamond machined to be optically flat. The bottom block had an overall flatness to within $5\mu m$ and
369   was ground to have a 3 μm r.m.s surface roughness. The longitudinal, c_L , and shear, c_S , wave velocities
370   were ultrasonically measured[44] under plain strain conditions. We obtained values of $c_p = 2680 \, m/s$ and
371     $c_s =$1361 m/s, with a $\pm$ 10 m/s error. This yields a Rayleigh velocity, c_R, of 1255 $\pm$ 10 m/s. The dynamic
372   Young's modulus and Poisson ratio are E=5.75$\pm$0.15 GPa and ρ =0.33$\pm$0.0007 respectively. The density
373   of the PMMA used was 1170$\pm$10 kg/m^3 Note that PMMA is viscoelastic. We measured the static Young's
374   modulus to be 3.62$\pm$0.3 GPa.

375   Barrier Construction
376   To create a surface barrier we used a Staedtler permanent marker of size M. The marker color was chosen
377   to be blue, which we found to be largely transparent to the blue (470nm) light used to illuminate the
378   interface. Prior to each set of experiments, we drew a line across the bottom block in the z direction
379   (normal to the propagation direction, x), and waited for an hour until the marker's solvent evaporated.
380   The effects of the marker could be erased by cleansing the interface with isopropyl alcohol.

381 We chose to implement different barrier widths between 1-4 mm. The barrier locations were changed
382 from set to set. Using an optical profilometer, we found that the thickness of the marker layer was
383 measured to be $< 1\mu m$ above the surface.
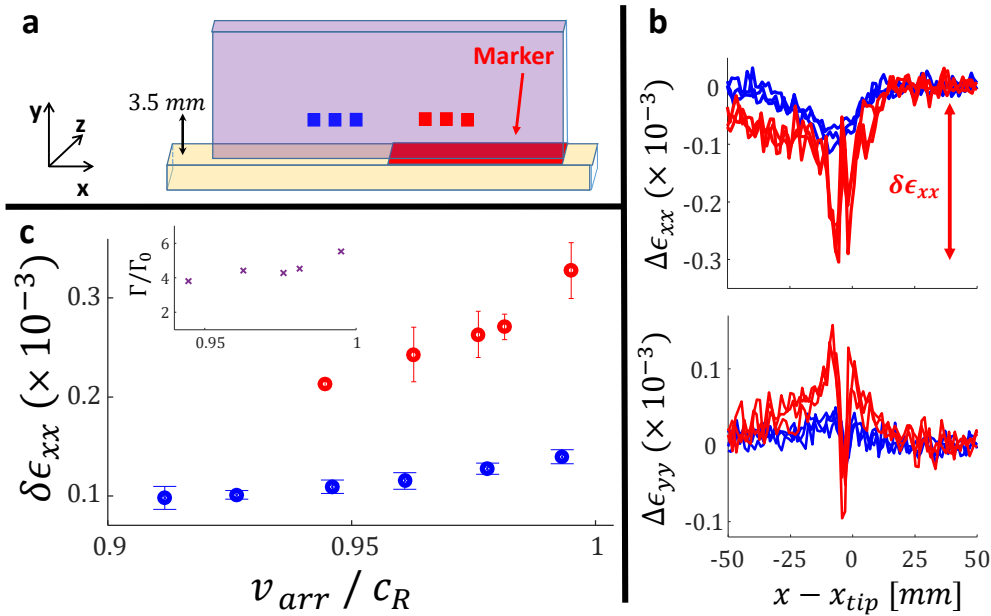
384

385 **Extended Data Figure 1: Fracture energy increase by the marker layer. a.** Schematic description of the experiment.
386 Half of the interface was painted with a marker layer, and the strain signals were measured by a number of rosette
387 type strain gages located about 3.5 mm above the interface. Blue (red) colors correspond to the bare (painted with
388 marker) interface, respectively. **b.** Comparison of the $\Delta \epsilon_{xx}$ (top) and $\Delta \epsilon_{yy}$(bottom) signals of the same rupture
389 front in the bare (blue) and painted (red) regions, respectively. This rupture front propagated at a velocity of
390 $1200\ m/s\ =\ 0.95 c_R$. Superimposed are 3 successive measurements spaced 7mm apart in both the bare (blue) and
391 painted (red) regions. The influence of the marker is evident on the amplitudes. Shown are (top) the $\Delta \epsilon_{xx}$ and
392 (bottom) $\Delta \epsilon_{yy}$ components, whose respective amplitudes $\delta \epsilon_{xx}$ and $\delta \epsilon_{yy}$ are proportional to the instantaneous
393 values of the stress intensity factor, K. **c.** $\delta \epsilon_{xx}$ as a function of the rupture velocity in both regions. Each point is an
394 average of 2-10 measurements; the error bars are their standard deviation. Colors denote the painted (red) and bare
395 (blue) sections of the interface. (inset) The resulting fracture energy ratios of painted and bare surfaces. Use of the
396 marker increases Γ on the interface by approximately a factor of 5.

397 The influence of the marker on the fracture energy along the interface was measured in separate
398 experiments, in which half of the top block was painted with the marker, while the other half remained
399 bare. The fracture energy, Γ, within each section was evaluated from the amplitude of the strain signals,
400 as measured by strain gages located about 3.5 mm above the interface, as in previous studies[1,2,39]. The
401 strain field amplitudes, are proportional to the instantaneous stress intensity factor, K, of the singular
402 component of the near-tip fields, as the rupture front traverses each strain gage[1]. As[1,24,45] $\Gamma \propto K^2$, we
403 have $\Gamma \propto \delta \epsilon_{xx}^2$, where $\delta \epsilon_{xx}$ is the maximal strain field amplitude. The results, presented in Extended Data
404 Fig. 1, show that the marker increases Γ by about a factor of 5.

405 <u>Loading system</u>
406 The loading system used was described, in detail, previously[1,15]. The top block was clamped at its top edge
407 and was pressed to the bottom block with an external force $F_N = 5000N$ in the y direction yielding a mean
408 normal stress of 4.5 MPa at the interface. F_N was maintained to be constant throughout each experiment.

409 The bottom block was mounted on a low friction translational stage, and stick slip behavior was achieved
410 by a quasi-static ($\sim 10 \mu m/s$ or about $50N/s$) loading of a shear force in the $-x$ direction. In all of the
411 events shown here, spontaneous cracks were nucleated near the $x = 0$ edge and propagated in the x
412 direction until arresting at the barriers. Note that, over the 1-10ms duration of these experiments, the
413 effects of the loading are negligible; the displacements and applied shear force varied, respectively, by
414 less than 1-10nm and 0.002-0.02%.

415 <u>Real contact area measurements</u>
416 Changes in the real contact area were measured by an optical method based on total internal reflection,
417 as light is transferred only at contact points[1,15,32,39]. The transmitted light intensity is proportional to
418 $A(x, z, t)$ and is continuously imaged at a 580000 frame/s rate with a spatial resolution of 1280×8 pixels
419 in the $x \times z$ directions. This translates to a mapping of $165 \times 688 \; \mu m/pixel$ in the x and z directions,
420 respectively. We illuminate the interface by means of a light sheet at a $70°$ incident angle that is
421 constructed using a high power LED (CBT 120) as a non-coherent light source to avoid interference
422 patterns and photoelastic effects. This incident angle is far from the critical angle ($\sim 42°$) for total internal
423 reflection from PMMA to air, so that nearly all of the light impinging on non-contacting area is reflected
424 away from the interface. The transmitted light, imaged by the camera, is therefore mapped to $A(x, z, t)$.

425 <u>v_{arr} determination</u>
426 Instantaneous rupture velocities were derived from the propagation of the tip location, which was defined
427 as the point where the value of $A(x, t)$ is decreased by 3%. The velocity of the rupture fronts when
428 reaching the barrier, v_{arr}, were measured by a linear extrapolation of the velocity measurements in the
429 preceding 15-20 mm to the barrier locations, x_0. This procedure yielded errors in the range of 20-30 m/s.
430 This uncertainty produced negligible errors in estimations of σ_{ind} except when $v_{arr} \to c_R$, where the
431 stresses σ_{ind} at the rupture tip become singular[24] as a function of $c_R - v_{arr}$. This increased uncertainty is
432 noted by the error bars within Fig. 4.

433 <u>Rupture edge detection</u>
434 $\xi(t)$ is defined as the leading edge of the rupture front in the x direction. To determine $\xi(t)$, we used
435 profiles, $\langle A(x, t) \rangle$, defined by $A(x, t)$, averaged over the z axis, and smoothed over a time interval ($\sim 20 \mu s$
436 for propagating fronts) where fluctuations of $A(x, t)$ were less than 200μm. The precise location of $\xi(t)$
437 was determined by fitting a second order polynomial (red line in Fig. 2b) to the $\langle A(x, t) \rangle$ profile of a region
438 ahead of the approximate front (we used a 1< $x - x_{app}$ <50mm range to perform these fits, where x_{app}
439 is the location of the approximated location). Our measurement noise is given by the standard deviation
440 of $A(x, t)$ around the fitted region. The rupture edge was defined as the location where the $A(x, t)$ profile
441 dropped 2 standard deviations below the extrapolated fit.

442 The average widths of the rupture, $\delta_z(t)$, were determined as follows. The nucleation patches generally
443 initiated near one of the interface's free faces, at either $z = 0$ or w. For each x location within the
444 propagating nucleation fronts, $\xi_0 < x < \xi(t)$, we chose the furthest point in z from the sample edge for
445 which A dropped by 2%. $\delta_z(t)$ was defined as the mean value of these measurements.

446 We note that for the $\delta_z(t)$ determination we used the center 6 out of the 8 rows measured in the z
447 direction, to avoid edge effects.

448 ### Damage Values, $\Delta A(t)$

449 We quantify the damage at the 'tail' of the nucleation front by averaging the changes in A within the
450 damage zone, as $\Delta A(t) \equiv 1 - \langle A(x,t)/A_0 \rangle_{z,x < \xi_0}$. The initial damage, D, was taken as the sharp jump in
451 ΔA within $10\mu s$ after the passage of the shear wave generated by the rupture arrest at the barriers.

452 ### τ determination

453 The nucleation time, τ, at which nucleation fronts became unstable was defined by the onset of sharp
454 acceleration in the $\xi(t)$ curve. This acceleration, which precedes dynamic rupture onset, is quite sharp,
455 with an uncertainty of less than $30\mu s$ for all experiments performed.

456 ### Induced stress, σ_{ind}, calculations

457 The induced stress field from the arrested crack was calculated using fracture mechanics. We used the
458 relations in (1) to obtain the static stress intensity factor of the arrested crack, K.

459
$$\Gamma = G_S \cdot g(v) = K^2/E \cdot (1 - \rho^2)g(v) \qquad (1)$$

460 In (1), ρ is the Poisson ratio and $g(v)$ is a universal dynamic function[24] that depends on the
461 instantaneous velocity, v, of the rupture front. G_S is the static energy release rate given by $\frac{K^2(v=0)}{E} \cdot (1 -$
462 $\rho^2)$. By determining K we could derive the induced stress field ahead of the crack, at all points, r, ahead
463 of the arrest location. Note that fracture mechanics provides not the stress, $\sigma_{xy}(r)$, at a point r but,
464 instead, the difference, $\Delta\sigma_{xy}(r) = \sigma_{xy}(r) - \sigma_{res}$, from the residual stress, σ_{res}, that remains after
465 rupture has taken place[29]. Once $K = \sqrt{(E\Gamma/(1-\rho^2))} \cdot g(v_{arr})^{-\frac{1}{2}}$ is determined from (1), then $\Delta\sigma_{xy}(r)$
466 is given by[24]:

467
$$\Delta\sigma_{xy}(r) = \sqrt{(E\Gamma/(1-\rho^2))} \cdot g(v_{arr})^{-\frac{1}{2}} \cdot (2\pi r)^{-\frac{1}{2}} \qquad (2)$$

468 The value of σ_{ind} at the nucleation point was defined as $\Delta\sigma_{xy}(r^*)$, where r^* is the distance from the
469 arrested crack tip to the nucleation point of the nucleation fronts. This location was approximated as the
470 center of the initial damage zone: $r^* \equiv L + \xi_0/2$, where L is the barrier width.

471 The values of r^* were, on average, constant in each set of experiments, with an uncertainty of about
472 $0.3\ mm$. The values $\sigma_{ind}(r^*)$ used in Fig. 4 were, therefore, determined using the average value of r^*.

473 ### Griffith length approximation

474 To determine the nature of slow propagation during the nucleation phase, we calculated the theoretical
475 Griffith length of a nucleation front of length l. Beyond a critical length of the nucleation front, fracture
476 mechanics predicts that crack propagation is governed by fracture mechanics. The critical value of K, K_c,
477 is determined by the measured fracture energy $\Gamma \cong 1\ J/m^2$; $K_c = \sqrt{((E\Gamma)/(1-\rho^2))}$. To this end, we
478 computed the theoretical static stress intensity factor, $K(l)$, of a shear crack of length l from the
479 nucleation location within our nucleation zone. For a one dimensional crack (in a 2D medium) $K(l)$ can
480 calculated using the Eshelby integral[24] with a (0.88) correction factor[46] for a center crack:

481
$$K(l) = 0.88\sqrt{\frac{2}{\pi l}} \int_0^l \frac{\Delta\sigma_{xy}(s)}{\sqrt{1-(s/l)^2}}\, ds \qquad (3)$$

482 Note that the integration starts from the nucleation point, which is located in the center of the damage
483 zone ($\xi_0/2$). We assume that the stress value, $\Delta\sigma_{xy}(s)$, at every nucleation front length, s, in the
484 integrand is that of the singular field given by (2) of the arrested crack at the barrier location, x_0 (e.g.
485 $\Delta\sigma_{xy}(s = 0) = \sigma_{ind} \equiv \Delta\sigma_{xy}(r^*)$).

486 Our nucleated crack fronts were **not** 1D through-cracks in a 2D medium. Instead, nucleated crack fronts
487 had an approximate elliptical shape in the xz plane of axis ratio $\delta/l = 0.85$. As a result, the computed
488 $K(l)$ from (3) had to be corrected[46,47] to account for this elliptical geometry. The elliptical crack shape
489 reduces the stress intensity factor, relative to a 1D center crack of the same length, resulting in an increase
490 of the Griffith length, L_G.
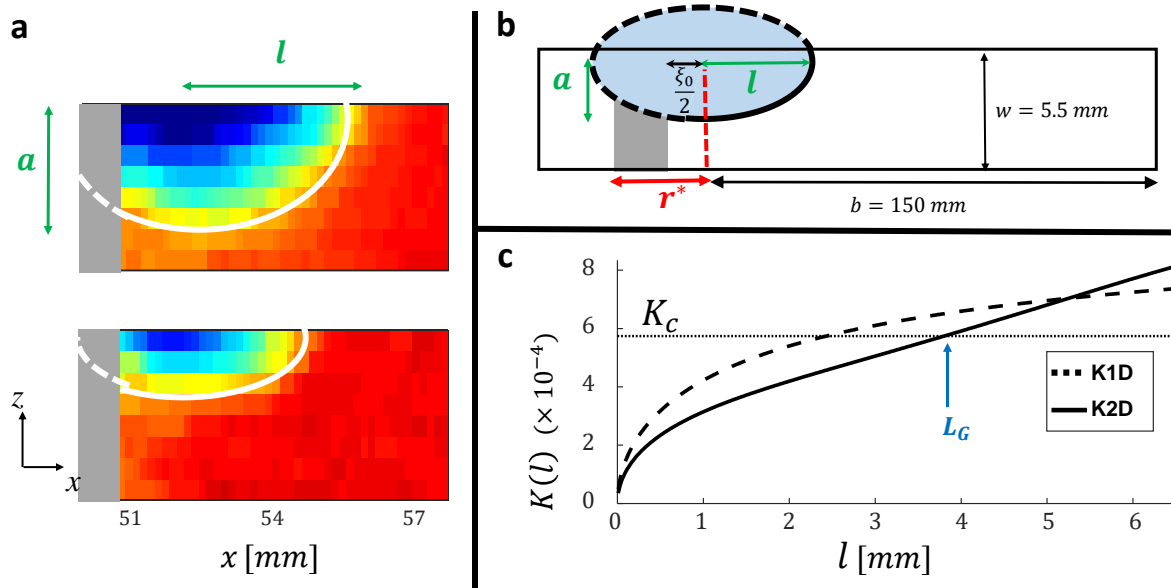
491

492 **Extended Data Figure 2. Calculation of theoretical stress intensity factors.** **a.** Two snapshots of the expanding
493 rupture during the nucleation phase of the event presented in Fig. 3. We can approximate the general shape of the
494 nucleating patch by a semi-elliptical edge crack[47], as denoted by the white line. The ellipse's axis ratio, a/l is
495 approximately 0.85, and remains fairly constant throughout the entire nucleation phase. **b.** Schematic description
496 of the calculation[47] of the stress intensity factor K, of a semi-elliptical edge crack. The parameters w and b used in
497 the calculation are noted. The nucleation patch was assumed to propagate in the x direction. The nucleation point
498 at the center of the ellipse, is located at the center of the initial damage zone, a distance of $\xi_0/2$ from the right edge
499 of the marker. The propagation distance, $l(t)$, used in the calculation is therefore $l = \xi(t) - \xi_0/2$ in terms of the
500 damage zone size, ξ_0 and nucleation front location, $\xi(t)$, which are both defined from the barrier edge (Fig. 3a). **c.**
501 The theoretical stress intensity factor as a function of crack length for the 1D (dashed line) and the elliptical (full line)
502 cases. The stress field used in this example is that denoted by the black line in Fig. 3c, where $v_{arr} = 1160\ m/s$. Note
503 that, experimentally, the onset of dynamic rupture (Fig. 3c) occurred at a length $l = 4$mm, which agrees well with
504 the predicted value ($l = 3.9$) for L_G. The dotted line denotes the critical stress intensity factor, K_c, above which
505 stationary cracks are unstable.

506 A comparison of $K(l)$ for the center crack (K1D in Extended Data Fig. 2c) and for the elliptical crack (K2D
507 in Extended Data Fig. 2c) is presented in Extended Data Fig. 2c. The parameters required for the
508 computation of this correction were the finite distance of $l = 0$ from the block's far edge (b=150mm), the
509 interface width (w=5.5), and the propagation direction, x.

510 The onset of fracture is dictated by energy balance, when the static energy release rate, $G_S(l) = K^2/E$
511 becomes equal to Γ, where E is the static Young's modulus for PMMA. The value of l, at the point of
512 instability is defined as the Griffith length, L_G. The values of L_G in our experiments are both significantly
513 greater than the lengths at which the slow propagation of the nucleation fronts initiate and are consistent
514 with the lengths of the nucleation fronts at the onset of dynamic rupture (at times $t = \tau$ in the text). For
515 example, using the measured value[1] of $\Gamma = 1\,J/m^2$, the calculated values of L_G for the 6 different
516 experiments performed at the barrier location of 50mm (much of the data presented in Figs. 2-5) yield
517 predicted Griffith lengths between 3.5 and 4 mm. This compares well to the corresponding **measured**
518 transition distances of 4 ± 0.25mm. This comparison is presented in Extended Data Figure 3. In the
519 experiment presented in Fig. 3c (black line), $\xi(t = \tau) \sim 5$ mm, where $\xi_0/2 \sim 1.2$mm (Fig. 2d- inset) so
520 $L_G = \xi(t) - \xi_0/2 \sim 3.8mm$.
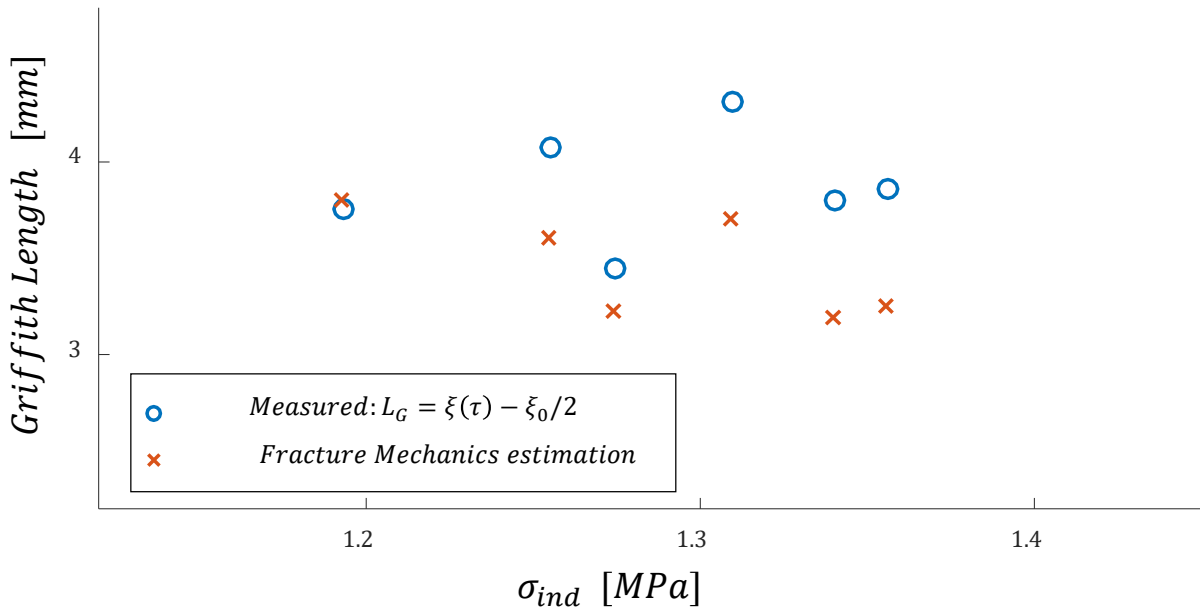
521
522 **Extended Data Figure 3.** Comparison of theoretical and measured Griffith lengths. Compared are the calculated
523 Griffith lengths, L_G with the measured distances of nucleation lengths, $\xi(\tau)$ from the nucleation locations, $\xi_0/2$.
524 The data shown correspond to the red data within Fig. 5a, in which nucleation fronts triggered rapid rupture fronts.

525 ## Critical nucleation length from Rate and State and Slip Weakening friction

526 ### Rate and State Friction

527 Calculations[43] of the stability of a steadily sliding block have been performed, assuming that the frictional
528 resistance τ is given by Rate and State friction[48,49]:

529 $\tau_{ss}(\sigma, V) = \tau_0 + f(\sigma) + \frac{(a-b)\sigma_0}{V_0}(V - V_0)$

530 where τ_0, σ_0 and V_o are, respectively, the shear stress, normal stress and sliding velocities in steady-state
531 frictional sliding. The value $a - b$ is defined by $a - b = \frac{V \partial \tau_{ss}(\sigma,V)}{\partial V}/\sigma$ where, V and σ are the block's
532 instantaneous sliding velocity and applied normal stress. For PMMA the values of the coefficients $a \sim$
533 0.008 and $b \sim 0.015$ have been independently measured[40,50,51] for our experimental conditions.

534 Rice et al.[43] derived a critical nucleation length at which steady sliding becomes unstable. This length is
535 given by:

536

$$L_c = \mu D_c \pi / [(b-a)\sigma_0]$$

538 In our experiments, the shear modulus, $\mu = 2GPa$, $\sigma_0 = 4.5MPa$, and the slip length D_c was obtained from
539 direct measurements of the cohesive zone size of propagating ruptures[39] yielding $D_c \sim 5\mu m$. Substituting
540 these quantities into the expression for L_c we find that $L_c \sim 1m$. This value is over two orders of
541 magnitude greater than the 4-8mm size (e.g. Fig. 5a in the text) of the measured nucleation lengths $\xi(\tau)$
542 in our experiments.

543 <u>Slip Weakening Friction</u>

544 Uenishi and Rice[37,52] calculated the critical nucleation length assuming a slip weakening friction law and
545 found that:

$$L_c = 1.158 \cdot \frac{\mu}{W} = 1.158\mu \cdot D_c / (\sigma_{peak} - \sigma_{res})$$

547 where σ_{peak} and σ_{res} are, respectively, the peak and residual frictional resistances of an interface. We
548 can relate these quantities to the fracture energy, Γ, which (in a slip weakening model) is given by $\Gamma = \frac{1}{2} \cdot$
549 $D_c(\sigma_{peak} - \sigma_{res})$. Substituting this expression into that for L_c and using the measured value of $\Gamma =$
550 $1J/m^2$, we find that $L_c = 7cm$ – or about an order of magnitude greater than the measured transition
551 lengths (3-8mm) to rapid ruptures that we have associated with the Griffith length.

552

553 <u>Linear scaling of τ^{-1} and σ_{ind}</u>

554 The linear relation between τ^{-1} and σ_{ind}, may be understood by combining the inertia-less dynamics of
555 the nucleation fronts with fracture mechanics.
556 Empirically, we find that $v_{nuc} \propto \sigma_{ind} - \sigma_{thresh} \equiv \beta(\sigma_{ind} - \sigma_{thresh})$, where σ_{thresh} is the threshold
557 stress for the onset of nucleation fronts (see Fig. 4). This linear relation could be expected from the class
558 of fluctuation-dissipation phenomena in which inertia-less motion takes place when forces are balanced
559 by dissipation. Examples of such phenomena include Stoke's drag in fluids or Ohm's law. In our case, the
560 stress, σ_{ind}, is balanced by the frictional resistance of the random contacts that compose the interface.
561 In the case of Stoke's flow or Ohm's law the external field driving the motion (gravity or an electric field)
562 is balanced by, respectively, random molecular motion or the interaction of charge carriers with random
563 impurities.
564 Using this, we can obtain a linear relation between τ^{-1} and σ_{ind} by simply invoking fracture mechanics.
565 We have shown that $\xi(\tau) - \xi_0/2 = L_G$ (L_G is the Griffith length). By definition, $v_{nuc} \cdot \tau = L_G$, so $L_G \propto$
566 $(\sigma_{ind} - \sigma_{thresh}) \cdot \tau$.
567 By fracture mechanics $L_G \propto \frac{K_c^2}{\sigma_{ind}^2}$ where K_c is a constant (given by the fracture energy).

568 Putting these expressions for L_G together, we obtain a prediction that $\tau \propto \frac{K_c^2}{\sigma_{ind}^2} \cdot (\sigma_{ind} - \sigma_{thresh})^{-1}$.

569 Since, for each experiment, σ_{ind} does not change drastically for each location, we find that $\tau^{-1} \propto \sigma_{ind} -$
570 σ_{thresh}, as indicated in Figure 4b.
571